Regenerative Therapy 26 (2024) 14–26

Contents lists available at ScienceDirect

Regenerative Therapy

journal homepage: http://www.elsevier.com/locate/reth

Original Article

Investigating the attenuating effects of metformin-loaded selenium nanoparticles coupled with *Myrtus communis* L. flower extract on CaOx deposition in male Sprague Dawley rat kidneys via regulating MAPK signaling pathway

Jian Kang [a], Yanqing Tong [b, *]

[a] School of Traditional Chinese Medicine, Changchun University of Chinese Medicine, Changchun 130021, China
[b] Department of Nephrology, The Affiliated Hospital to Changchun University of Chinese Medicine, Changchun 130021, China

ARTICLE INFO

Article history:
Received 3 February 2024
Received in revised form
4 April 2024
Accepted 11 April 2024

Keywords:
Myrtus communis L.
Metformin
Se NPs
CaOx crystals
ECM deposition
MAPK signaling pathway

ABSTRACT

Kidney stones are a foremost clinical concern in urology with CaOx crystals accounting for roughly 80% of these renal formations. This research endeavor seeks to ascertain the protective effects of Metformin-encapsulated selenium nanoparticles (M@Se NPs), combined with a 55% hydroethanolic flower extract from *Myrtus communis L.* (*MCL*) in countering the formation of kidney stones in Male Sprague Dawley rats. The particle's diameter was measured to be 39 nm and 13.8 nm from DLS and HR-TEM analysis. Rat groups administered with the *MCL*-M@Se NPs (1:1.5:1) exhibited reduced renal stone formation in urine and serum analysis compared to the negative control group. Histological evaluations of kidney samples using H&E, and MTS staining indicated a subdued presence of ECM deposition in contrast to other rat groups. Conclusively, the protective mechanism of *MCL*-M@Se NPs against CaOx stone damage can be confidently attributed to the obstruction of the MAPK signaling pathway.

1. Introduction

Renal lithiasis, a urological disorder, arises from a typical aggregation of crystalline substances like uric acid, oxalate, and calcium within the kidney [1]. This ailment prevalently impacts approximately 1–5% of the Asian demographic, 5–9% of the European cohort, and 7–13% of the North American populace, making it a globally pervasive health concern. Primarily, conditions like diabetes, hypertension, hyperparathyroidism, and obesity predispose individuals to the formation of kidney stones [2,3]. Additionally, these stones can precipitate multiple complications, including infections, localized renal damage, renal dysfunction, and obstructions in the urinary tract [4]. Over the past few decades, surgical interventions for excising kidney and ureteral stones have seen substantial advancements and refinement. Despite the advancements in surgical treatments effectively mitigating postoperative complications, the persistent high recurrence of stones remains troubling [5,6]. Consequently, researchers are delving into novel medications and targets that are imperative to diminish both the recurrence and incidence of kidney stones.

Metformin, a biguanide antidiabetic drug in use since 1958 is the most frequently prescribed medication for type II diabetes worldwide. Beyond its primary purpose, it offers a plethora of benefits such as cancer risk reduction, enhanced antioxidant defense, and life extension [7,8]. Though conventionally prescribed for diabetes, recent studies have illuminated its multifaceted benefits, encompassing wound healing enhancement, oxidative stress reduction, and stroke risk mitigation [9]. Notably, metformin demonstrates promising attributes for kidney protection. It not only mitigates renal fibrosis and decreases urinary protein concentrations but also showcases protective effects against kidney stone formation through its antioxidant actions [10]. Metformin further postulated that metformin hinders the progression of calcium oxalate kidney stone formation, examining potential pathways linked to MCP-1 and OPN [11,12]. Nonetheless, the precise processes through which metformin counteracts calcium oxalate crystallization and curtails reactive oxygen species generation, thus alleviating renal oxidative stress are yet to be comprehensively

* Corresponding author. NO. 1478, Gongnong Road, Chaoyang District, Changchun 130021, Jilin Province, China.
E-mail address: Yanqing_Tong@hotmail.com (Y. Tong).
Peer review under responsibility of the Japanese Society for Regenerative Medicine.

https://doi.org/10.1016/j.reth.2024.04.006

elucidated. While metformin has been researched for its potential to reduce renal stone formation long-term usage has been linked to mild adverse effects [13–15]. As a result, the present study introduces a novel approach such as the conjugation of metformin with phytochemicals present in medicinal herbs. This strategy aims to harness the therapeutic potential of both metformin and these natural compounds, possibly enhancing efficacy and minimizing side effects.

In general, medicinal plants have long been pivotal in both ancient and contemporary medical systems. As a result, compounds derived from these plants present therapeutic avenues potentially advantageous for a large segment of the global populace [16]. Additionally, procuring active constituents from plants is cost-effective, and these constituents typically exhibit milder side effects than many modern pharmaceuticals [17]. Furthermore, the extraction of alkaloids and phenolic compounds from plants is considered an environmentally friendly approach with commendable efficacy. Scientific examinations of medicinal plants used in traditional anti-nephrolithic treatments have demonstrated promising outcomes in both *in vitro* and *in vivo* studies [18].

Myrtus communis L. (*MCL*) is a renowned herb in traditional Chinese medicine celebrated for its efficacy in treating a range of conditions including inflammation, ulcers, diarrhea, and disorders of the respiratory and digestive systems [19]. Integral to *MCL*'s therapeutic value are its components, particularly phenols and antioxidants. The most extensively researched phenolic constituents of myrtle encompass flavanols, flavonols, and anthocyanins [20]. Notably, phloroglucinols, such as myrtucommulone and semi-myrtucommulone have garnered attention in the context of myrtle due to their distinct antibacterial and antioxidant activities. Previous empirical studies have underscored the antioxidant and anti-inflammatory attributes of *MCL* leaves with evidence drawn from mouse paw edema, liver fibrosis, granuloma, pulmonary fibrosis, colonic inflammation, and ear edema in rat models [21,22]. The selection of *Myrtus communis* L. flower extract was based on its powerful antioxidant and anti-inflammatory characteristics which are essential in the fight against CaOx stone formation. Previous research has proven that it can prevent the production of crystals and decrease oxidative stress which makes it a hopeful option for managing kidney stones. Given this data, it is anticipated that the ethanol extract of *MCL* leaves could offer a promising avenue in thwarting the onset of kidney stones.

Selenium is a crucial trace mineral that plays a pivotal role in preserving the integrity and functionality of the kidneys. A deficiency in this element can compromise the ultrastructural components of renal tubules, glomeruli, and the extracellular matrix [23]. Both *in vitro* assessments and clinical research illustrate that selenium supplementation can counteract the development of urolithiasis. However, inorganic selenium presents challenges such as instability and dosage regulation complexities [24]. In contrast, phytochemicals with their abundant sources, amendable structures, robust stability, multifaceted biological activities, and minimal toxicity, offer an attractive alternative. Similarly, sodium selenite can thwart urolithiasis due to its affinity for crystal surfaces, thereby curbing CaOx crystal accumulation, expansion, and inception [25]. The appropriate concentration of selenium nanoparticles, often referred to as crystallization inhibitor molecules might avert crystal genesis from supersaturated solutions. Numerous studies suggest that combining Se NPs with phytochemicals found in extracts can not only reduce toxicity but also amplify their therapeutic efficacy [26]. For instance, Ganapathy et al. [27], developed spherically structured Se NPs using *Brassica oleracea (broccoli)* extract as a reductive agent. They evaluated the antibacterial potency of these NPs against five distinct bacterial strains: *E. faecalis, S. aureus, Lactobacillus* sp., *S. mutans,* and *C. albicans*. Remarkably, the *Brassica oleracea*-Se NPs boasting an average particle diameter of 15.2 nm, exhibited enhanced antibacterial performance as evidenced by larger zones of inhibition. Similarly, Lokanadhan et al. [28], prepared phyto-fabricated Se NPs (PF–Se NPs) using aqueous fruit extract of *Emblica officinalis*. The Se NPs were elucidated with the average particle size of 15–40 nm from HR-TEM analysis and zeta potential of −24.4 mV from DLS analysis. Additionally, PF-Se NPs showcased remarkable stability, nano-dimensional scale, and a spherical configuration. These nanoparticles have demonstrated significant bio-functional potentials, encompassing antioxidant, antimicrobial, and biocompatible activities. Notably, the PF-Se NPs exhibited formidable free radical neutralizing capabilities proving to be more efficient than the benchmark antioxidant and ascorbic acid. Likewise, research by Swetha Reddy Vundela et al. [29], focused on the fabrication of Se NPs leveraging *Carica papaya* extract and delving into their multifaceted biological attributes. These Se NPs maintained stability as evidenced by a Zeta potential of −32 mV. Their antimicrobial prowess spanned a wide spectrum with the inhibition hierarchy being most pronounced for fungi followed by Gram-positive bacteria, and culminating with Gram-negative bacteria. Furthermore, these Se NPs demonstrated a selective predilection for curtailing the growth of cancerous cells specifically targeting IMR-32, Caco-2, RAW 264.7, and MCF-7 cells. In contrast, their impact on benign cells like Vero was relatively benign, underscoring their commendable biocompatibility. Manosi Banerjee et al. [30], proposed a facile and eco-friendly approach for synthesizing Selenium nanoparticles with the aid of *Moringa oleifera* leaf extract from Sodium Selenite solution. The research group demonstrated that Se NPs were effective in *Pseudomonas aeruginosa* biofilm formation. Similarly, Shabnam Tamanna et al. [31], synthesized Se NPs with *Orthosiphon stamineus* leaf extract in a greener way and utilized them for biomedical applications. The obtained results justify that the formulation only exhibited 5% lysis at 100 μg/mL in hemocompatibility studies. The findings suggest that the Se NPs synthesized utilizing a greener method would be biocompatible compared to other synthesis protocols. Collectively, the research indicates that Se NPs, when produced using plant extracts and possessing a particle size ranging between 10 and 20 nm coupled with elevated negative zeta potential values demonstrate pronounced antioxidant activity.

In this study, Metformin-encapsulated with selenium nanoparticles (M@Se NPs), combined with flower extract from *Myrtus communis* L. (*MCL*) were synthesized. This present article also aims to prove the mechanism of action laid behind the protective effect of *MCL*-M@Se NPs on kidney stones induced in male Sprague Dawley rats. The physicochemical characterization of the synthesized *MCL*-M@Se NPs was validated using Ultraviolet–visible (UV–Vis), Fourier-transform-infrared (FT-IR), Dynamic light scattering (DLS), X-ray diffraction (XRD), High Resolution-Transmission Electron Microscopy (HR-TEM) and X-ray photoelectron spectroscopy (XPS) spectroscopy. Importantly, the inhibitory effects of *MCL*-M@Se NPs were elucidated with histological evaluations such as H&E, and MTS staining with other rat groups. Similarly, the expression markers such as Cleaved caspase-3, p-ERK1/2, Raf1, and p-MEK1 were evaluated along with their respective mRNA expression in rats treated with *MCL*-M@Se NPs in comparison to other rat groups. This research endeavored to furnish conclusive proof for the formulation of innovative, clinically viable *MCL*-M@Se NPs for use as anti-urolithiasis agents.

2. Materials and methods

2.1. Preparation of Myrtus communis L. flower extract by Soxhlet's extraction method

Initially, fresh *Myrtus communis* L. flowers were harvested, rinsed twice using deionized water, and then shade-dried for 15

days. *Myrtus communis* L. flowers that had been dried were ground using an electric mixer until they turned into a fine powder which was then utilized for extraction purposes. Carefully, 15 g of this powdered *Myrtus communis* L. flower was encased in Whatman filter paper, positioned in the thimble, and subsequently introduced into the Soxhlet extraction apparatus. The extraction process was set for a duration of 48 h until the solvent reached its boiling point using a mixture of 100 mL of water and analytical grade ethanol as extracting solvents. The resulting 55% hydroethanolic extract from *Myrtus communis* L. flowers underwent filtration using a 20–25 μm Whatman filter paper in a reduced-pressure environment. For further refinement, any residual fine particles left in the solution were eliminated through centrifugation at 2500 rpm for 10 min. The purified extract was then preserved at 4 °C for future use.

2.2. Synthesis of MCL-M@Se NPs

The research employed Sodium selenite (Na_2SeO_3) as a source of selenium, diluted to a 10 mM concentration using deionized water to achieve a total volume of 20 mL. In beaker-A, an extract from the flower of *Myrtus communis* L. (15 mL) was introduced. Subsequently, the Na_2SeO_3 solution was incrementally introduced while ensuring consistent agitation at a temperature of 70 °C. Concurrently, in Beaker-B, Metformin tablets (molecular weight of 84.08) were pulverized using a mortar and pestle and then suspended in deionized water to yield a 10 mM solution. This freshly prepared metformin suspension was then added with the contents of Beaker-A with stirring sustained for an additional 30 min. The emergence of Se NPs was discernible by a noticeable red colour in the solution. The solution was subjected to centrifugation at 1500 rpm for 3–4 min. This procedure segregated the larger Se-NPs, leaving behind in the supernatant a solution of *MCL*-M@Se NPs. Employing an analogous methodology, the comparative effectiveness of *MCL*-M@Se NPs was evaluated against metformin@Se NPs (M@Se NPs) and *Myrtus communis* L. flower extract@Se NPs (*MCL*@Se NPs). The primary distinction in the protocol was the exclusion of *Myrtus communis* L. flower extract when synthesizing M@Se NPs, and the absence of metformin in the creation of *MCL*@Se NPs (Fig. 1).

2.3. Experimental design

The Changchun University of Chinese Medicine, Changchun ensured that all protocols related to animal experimentation, ensuring they adhered to the highest ethical standards for animal welfare. Sprague-Dawley male rats (n = 50) aged 6 weeks and weighing between 150 and 220 g were employed for the study. These rats were nourished with standard commercial rat feed and given regular water; all while being housed in a controlled humidity environment. Additionally, the cage flooring was layered with sawdust to prevent potential illnesses and ensure optimal cleanliness. Following a 4-week acclimation phase, the rats were arbitrarily segregated into five uniform groups. Group A: healthy control, Group B: negative control, Group C: rats administered M@Se NPs, Group D: rats given *MCL*@Se NPs, and Group E: rats treated with *MCL*-M@Se NPs (1:1.5:1). Group A, the healthy control was provided distilled water in place of tap water for 28 days. The subsequent groups were given 3 mL of a solution composed of 1% ethylene glycol and 2% ammonium chloride as a substitute for water, administered daily via gavage for 28 days. Group B functioned as the negative control. Group C, labeled M@Se NPs was subjected to daily intraperitoneal injections starting on day 14. In a parallel manner, Group D denoted as *MCL*@Se NPs, underwent intraperitoneal injections daily between days 15 and 28. Group E, termed *MCL*-M@Se NPs consistently received their 1 mL dosages from days 15–28. 24 h before euthanasia, urine specimens were procured from all the rats and preserved at −80 °C. Subsequently, on the 28th day, the rats were administered anesthesia (Xylasin/Ketamine = 0.45/10 mg kg^{-1}). Blood samples were drawn, and then centrifuged at 4000 rpm for 15 min at a temperature of 4 °C. The resulting serum supernatant was carefully siphoned off and retained at −80 °C. Post euthanasia, the left renal organ was fixated in a 4% paraformaldehyde solution and subsequently encased in paraffin for hematoxylin, eosin (H&E), and Masson's trichrome staining procedures. In contrast, the right renal organ was instantly frozen using liquid nitrogen and maintained at −80 °C.

2.4. Collection and analysis of urine and serum samples

After a 28-day observation period, rats were situated in metabolic cages for 24 h urine sample collection. These specimens were contained in tubes with 0.02% sodium azide to deter bacterial proliferation. After ascertaining their volume and pH, the samples were partitioned for a range of assessments, specifically for magnesium (MAK026-sigma Aldrich), phosphate (MAK308-sigma Aldrich), nitrogen (MAK449-sigma Aldrich), oxalate (MAK315-sigma Aldrich), calcium (MAK022-1 KT-sigma Aldrich), and uric acid (MAK077-sigma Aldrich). The evaluations employed commercial assay kits adhering to the directives provided by the manufacturer, and measurements were conducted using the Varioskan Flash microplate reader by Thermo Scientific. After that, sedatives were given to the rats, and blood samples were quickly

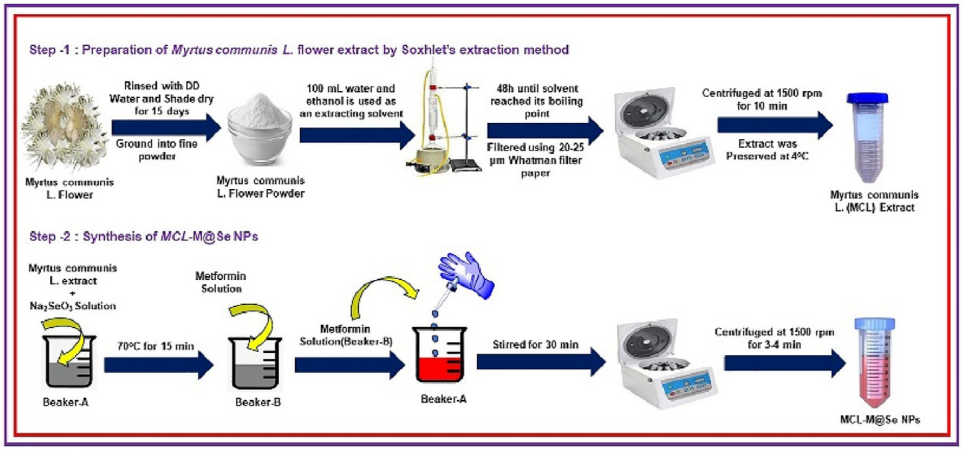

Fig. 1. Schematic illustration on the synthesis of Metformin-Loaded Selenium Nanoparticles Coupled with *MCL* Flower Extract.

taken from the orbital sinus. These samples were placed into centrifuge tubes without anticoagulants. Once the blood samples coagulated naturally, they were centrifuged according to the above-discussed protocol to isolate the serum. This serum was then analyzed for its creatinine and nitrogen content. Additionally, the serum levels of tumor necrosis factor-α (TNF-α), interleukin-6 (IL-6), and interleukin-1β (IL-1β) were ascertained using Enzyme-Linked Immunosorbent Assay (ELISA) Kits sourced from Thermo Fisher Scientific. The assay was diligently performed in line with the manufacturer's instructions stipulated in the ELISA kit.

2.5. Histopathological and immunohistochemistry studies

2.5.1. H&E staining

The renal tissues fixed in 4% paraformaldehyde were subjected to a sequential dehydration procedure using ethanol [32]. Post-dehydration, the tissues were immersed in xylene for 30 min. After this immersion, they were encased in paraffin. Slices of these encased tissues, varying from 3 to 5 μm in thickness were carefully sectioned. These tissue sections were subsequently stained with Hematoxylin and Eosin (H&E). Utilizing a BA210 LED Digital microscope (magnification 200×), scrupulous examinations were conducted to observe histopathological alterations in the renal structure and to detect calcium oxalate deposits.

2.5.2. Masson trichrome staining

Paraffin-embedded kidney tissue sections were first dewaxed with xylene and subsequently rehydrated through a graded series of alcohols. These sections were then subjected to α-SMA and COL1A1 primary antibodies and incubated at 4 °C overnight. To eliminate any non-bound primary antibodies, the sections underwent a buffer rinse. They were then exposed to an appropriate secondary antibody, either coupled with a colorimetric or fluorescent marker, diluted in an appropriate solution. After the stipulated incubation time, another buffer rinse was performed to discard any residual unbound secondary antibodies. Interestingly, kidney tissues were preserved in 4% paraformaldehyde for a day at 4 °C, then encased in paraffin and sectioned. Each section was then rinsed three times with distilled water each wash lasting 5 min. Utilizing the Trichrome Stain (Masson) Kit from Sigma Aldrich, solution A was introduced and left to act at room temperature for 12 h. The sample slices submerged in the solution were then heated in an oven at 60 °C for 30 min, after which solutions D and F were added for the preheating process. Following this, the specimen was washed with tap water until the yellow tint on the tissue dissipated. Equal portions of solutions B and C were combined and utilized to stain the specimens at 35 °C. Afterward, they were once again rinsed with tap water. Post-treatment of the specimen with a mixture of 1% hydrochloric acid and alcohol for a minute resulted in the nucleus acquiring a grayish-black shade. Following a tap water rinse, the specimen was stained with solution D for approximately 5 min. After another wash, it was subjected to staining with solution E at 35 °C. Without an intervening rinse, the specimen was subsequently stained with solution F at ambient temperature. The differentiation phase encompassed treating the sample with 1% glacial acetic acid thrice each session lasting a few minutes. Renal fibrosis was identifiable by the blue areas evident in the Masson trichrome staining [33]. All microscopic observations were conducted using a Nikon light microscope with captured images further scrutinized using ImageJ software.

2.6. Detection of SOD, MDA, CAT, GPx, GSH, and GR in renal tissue

For the identification of SOD, MDA, CAT, GPx, GSH, and GR, a precise 1 g of kidney tissue was meticulously placed in a mortar and pulverized with a pestle using a precooled homogenizing buffer containing 0.9% sodium chloride (1:9) on an ice bath. This was rigorously mixed using a pipette for approximately 8–10 min until the tissue was thoroughly homogenized. The resultant 10% homogenate was then subjected to centrifugation at a gentle speed of 500 rpm for 10 min in cold conditions [34]. Following this, the supernatant was carefully decanted and mixed with the specific reagents provided in the detection kit, adhering to the stipulated guidelines. In the final step, the optical density (OD) readings were acquired using an Agilent BioTek Synergy Neo2 Hybrid Multimode Reader.

2.7. Western blotting analysis

Proteins were extracted from renal tissues utilizing RIPA buffer, and their quantitative levels were ascertained via a BCA protein assay kit sourced from Sigma Aldrich. Subsequently, these proteins underwent separation through a 10% SDS-PAGE process and were translocated to PVDF membranes. Post this step, the membranes were subjected to blocking via a 5% non-fat milk solution for 3 h under ambient conditions. These membranes were then incubated with primary antibodies such as Raf1, ERK1/2, p-ERK1/2, MEK1, p-MEK1, and Cleaved caspase-3, allowing them to remain in this state at 4 °C throughout the night. After a trio of washes, they were exposed to secondary antibodies for 3 h at a temperature of 35 °C [35]. Visualization of protein bands was facilitated through a chemiluminescence method with their relative densities being quantified using the ImageJ software, benchmarking against β-actin.

2.8. Quantitative RT-PCR analysis

To corroborate the insights garnered from our RNA-seq analysis, we utilized quantitative real-time RT-PCR to assess six selected genes. We orchestrated these experiments across three biological replicates for each category. The gene-specific primers were conceived using the Primer Premier 5.0 software, and a comprehensive detailing of these genes alongside their respective primers is furnished in Table 1. The RT-PCR was operationalized on the Light Cycler 480 instrument-II with a reaction mixture of 10 μL, incorporating 5 ng of the cDNA template and the SYBR Premix Ex Taq II. The procedure was initiated with a 5-min pre-incubation at 98 °C, succeeded by 45 cycles at 98 °C for 20 s, then transitioning to 60 °C for 50 s [36]. Upon completion of amplification, we scrutinized the melting curve to validate the singular product amplification. Concurrently, during the 60 °C, 50-sec segment of each cycle, we documented fluorescence signals via the LightCycler 480 instrument-II. Expression magnitudes of the focal genes with β-actin were ascertained employing the $2^{-\Delta\Delta Ct}$ methodology.

Table 1
Primers of the 6 gene sequences.

C-Raf	F-5′-TGAAAAGGTTGGTGGCTGACTG-3′
	R-5′- CGGTTTATCTTAGGGAGGGCAT-3′
MAPK1	F-5′-TGGTTCCTCCCACTCCTGAA-3′
	R-5′-TGGGCAAATAGCACACACCT-3′
MAPK3	F-5′-ACTACCTGGACCAGCTCAAC-3′
	R-5′-GCTTGTTGGGGTTGAAGGTT-3′
MAP2K1	F-5′-TGGTGGCAGATGTAGTAGT-3′
	R-5′-ATTGCTCGTCCTTACCATTC-3′
MAP2K2	F-5′-ACTCGTGCAGCACCTGCA-3′
	R-5′-TGCA GGTCGT CAGCGAGT-3′
CASP3	F-5′-GCAGCTTTGTGTGTGTGATTC-3′
	R-5′-AGTTTCGGCTTTCCAGTCAG-3′

2.9. Statistical analysis

All findings are delineated as the average ± standard deviation (SD). Analytical processing of the data was orchestrated using the GraphPad Prism software, and distinctions among the quintet of groups were scrutinized via one-way ANOVA. For individual pairwise analyses, the LSD-*t* test was invoked under conditions of consistent variances, whereas Tamhane's T2 test was harnessed for disparate variances. A statistical significance threshold of $P < 0.01$ was established.

3. Result and discussion

3.1. UV visible analysis

The UV–vis spectrum depicted in Fig. 2a underscores the existence of phytochemicals in *MCL* flower extract and the synthesis of Se NPs within *MCL*-M@Se NPs. Primarily, the *Myrtus communis* L. plant, renowned for its rich flavonoid content is a staple in Unani medicine. A spectral peak at 233 nm suggests the presence of compounds such as terpenoids, saponins, tannins, and alkaloids in the 55% hydroethanol-based *MCL* flower extract, all of which are reputed for their antioxidant attributes [37]. In contrast, a peak approximately at 334 nm is associated with the metformin medication. Upon merging the *MCL* flower extract with the metformin drug in the presence of Se-precursor, a new peak at 273 nm emerges in the *MCL*-M@Se NPs. This spectral shift is paralleled by a hue transition from yellow to deep crimson in the solution, signifying the genesis of Se NPs. Importantly, the inherent phytochemicals in the *MCL* flower extract combined with metformin facilitate the straightforward reduction of Se NPs, obviating the need for extrinsic reducing agents such as hydrogen peroxide or sodium borohydride. This hue metamorphosis signifies the surface plasmon resonance inherent to Se NPs, which arises from the transformation of Se^{4+} to Se^{0} NPs [38,39]. It's pivotal to recognize that a more acute wavelength and a broader peak hint at the Se NPs within *MCL*-M@Se NPs being both spherical and diminutive in dimension.

3.2. FT-IR analysis

FT-IR spectroscopy is an advanced analytical method employed to identify the specific chemical bonds within a substance by gauging the absorption of infrared light (Fig. 2b). The *Myrtus communis* L. extract revealed a multitude of absorption peaks at varied positions. Specifically, the peak around 3436 cm^{-1}, as well as those at 2926 and 2848 cm^{-1} can be attributed to the hydroxy group and the symmetrical and asymmetrical stretching modes of −CH, respectively. The peak at 2069 cm^{-1} is indicative of the C≡C stretch. Additionally, the stretching frequencies at 1701 cm^{-1}, 1369 cm^{-1}, and 1024 cm^{-1} are associated with the carbonyl stretch C═O and the C–O stretch both of which are related to various oxygen-containing functional groups [37,40]. The FT-IR spectrum of unadulterated metformin as illustrated in Fig. 2b, exhibits characteristic peaks at 3269, 1642, and 1072 cm^{-1}. These peaks are attributable to primary N–H stretching and C═N stretching modes, respectively. The FT-IR spectrum of the biosynthesized *MCL*-M@Se NPs reveals a pronounced absorption peak at 3263 cm^{-1}, signifying the presence of −OH groups. This subtle wavenumber shift can be attributed to the incorporation of Se NPs within the *MCL*-M@Se NPs structure. Additional peaks surface at 2913 cm^{-1}, indicative of aldehyde groups; 2140 cm^{-1}, corresponding to the C–N group; and 1642 and 1523 cm^{-1}, pinpointing the existence of carbonyl groups [38]. A faint band around 1392 cm^{-1} is suggestive of the aliphatic bending group while 1237 cm^{-1} denotes the alkyl ketone group, and 1002 cm^{-1} points to the presence of alkyl amine groups. The C–H groups are identified by the wavenumber at 532 cm^{-1}. The detection of the alkyl ketone group substantiates the inclusion of flavonoids as part of the phytochemicals in the *MCL* flower extract [41]. These flavonoids possess a myriad of functional groups that play a pivotal role in the bioreduction of Se NPs [42]. The emergence of alkyl amine groups underscores the role of the *MCL* flower extract which carries the $-NH_2$ group, in both the bio-reduction and stabilization of the nanoparticles.

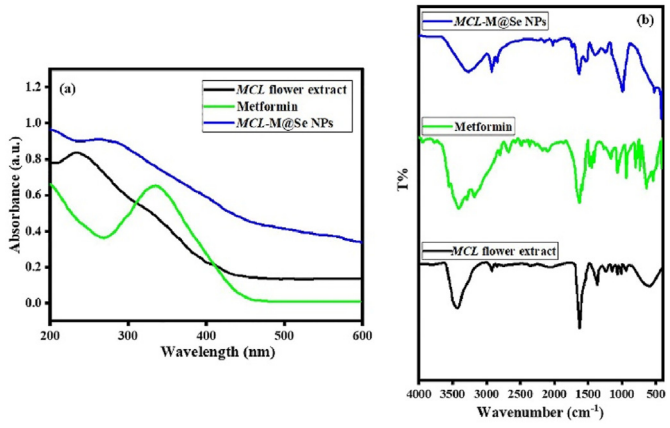

Fig. 2. UV–visible spectrum (a) and FT-IR spectrum (b) for *MCL* flower extract, metformin and *MCL*-M@Se NPs.

3.3. XRD analysis

The XRD analysis of *MCL*-M@Se NPs is presented in Fig. 3a alongside a simulated reference pattern. Typically, XRD is utilized to determine aspects like crystalline size, microstrain, and lattice parameters. The simulated reference for Se NPs labeled with JCPDS No: 06-0362 shows ten distinct peaks in Fig. 3a. The XRD pattern of *MCL*-M@Se NPs aligns well with this simulated reference for Se NPs [43]. Notably, a subtle shift towards higher diffraction angles in the spectrum is observed. This could be attributed to the formation of smaller nanoparticles that might have more lattice contraction than the bulk Se NPs. Using the Debye Scherrer equation $\left(crystalline\ size = K\lambda/\beta\ cos\ \theta\right)$, the crystalline size of Se NPs in *MCL*-M@Se was found to be 48 nm. Given that K is a constant, valued at 0.94, β represents the FWHM, θ symbolizes the diffraction angle, and λ signifies x-ray radiation wavelength [44]. Such contraction can lead to diminished interplanar spacing, subsequently causing a migration of the XRD peaks towards higher angles. Moreover, the biologically synthesized Se NPs when combined with the metformin drug showed a decrease in crystalline size due to the templating effect and synergistic actions. Furthermore, the incorporation of metformin drugs, flavonoids, and alkaloids results in lattice contraction which correlates with the smaller size of Se NPs in *MCL*-M@Se NPs.

3.4. DLS analysis

Laser diffraction analysis was employed to examine the particle size distribution and zeta potential of the produced nanoparticles. Fig. 3(b-g) depicts the particle size distribution and zeta potential for M@Se NPs, *MCL*@Se NPs, and *MCL*-M@Se NPs. Specifically, the particle sizes were determined to be 51 nm for *MCL*@Se NPs, 59 nm and 336 nm for M@Se NPs, and 39 nm for *MCL*-M@Se NPs (Fig. 3(b-d)). It's important to note that the decrease in particle size is

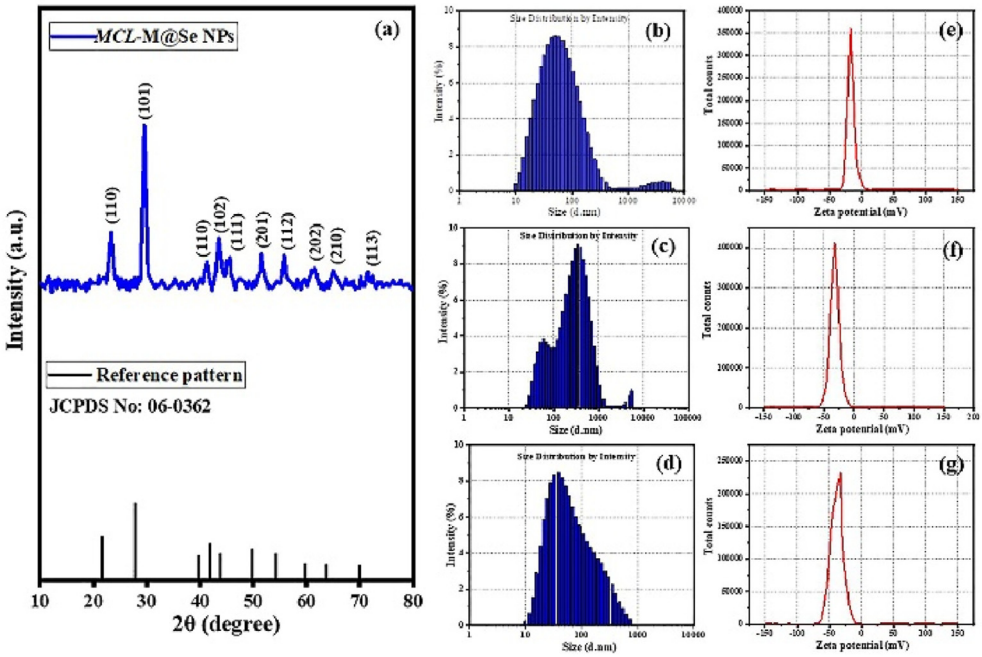

Fig. 3. XRD spectrum of *MCL*-M@Se NPs along with stimulated reference pattern (a), size distribution (b–d) and zeta potential (e–g) results from DLS spectroscopy for *MCL*@Se NPs, M@Se NPs and *MCL*-M@Se NPs.

attributed to the templating effects and synergistic actions of the *MCL* flower extract combined with the metformin drug [45,46]. Indeed, the phytochemicals and the amine (-NH_2) group facilitate a more effective reduction of the Se NP while the flavonoids present in the *MCL* extract act as templating agents. In parallel, the zeta potential measurements indicate negative values: −16 mV for *MCL*@Se NPs, −29 mV for M@Se NPs, and −32 mV for *MCL*-M@Se NPs (Fig. 3(e-g)). A heightened negative charge suggests robust stability for the Se NPs preventing aggregation particularly in the *MCL*-M@Se NPs.

3.5. HR-TEM analysis

High-resolution Transmission Electron Microscopy (HR-TEM) was employed to determine the size of Se NPs within the synthesized *MCL*-M@Se NPs. HR-TEM images are presented in Fig. 4a–d with magnifications ranging from 200 nm to 10 nm. Notably, the *MCL*-M@Se NPs reveal distinctively spherical morphologies of selenium nanoparticles, corroborating the data obtained from UV–visible spectra. The particle size histogram (inset of Fig. 4c) reveals an average particle size of 13.8 nm for the Se NPs. Additionally, d-spacing value of 0.33 nm was computed for the Se NPs within *MCL*-M@Se NPs (Fig. 4d). It's important to note a discernible discrepancy in Se NP sizes when analyzing DLS. This stems from the fact that DLS evaluates the hydrodynamic size of nanoparticles in tandem with any associated chemicals, whereas HR-TEM solely gauges the physical size of Se NPs [47,48]. The diminutive size of these particles can be ascribed to the enhanced reductive capabilities and synergistic effect of the employed *MCL* flower extract and the metformin drug. This reduction in particle size was crucial in bolstering the anti-urolithiasis efficacy in the Sprague Dawley rat model.

3.6. XPS analysis

The XPS analysis of the synthesized *MCL*-M@Se nanoparticles was conducted to assess the presence of Se nanoparticles and their specific spin states. Notably, the Se 3d core level spectrum exhibits four prominent peaks. Two of these, positioned at 55.03 eV and 55.79 eV, can be ascribed to the Se $3d_{5/2}$ and $3d_{3/2}$ states [49]. Likewise, the additional two peaks situated at 56.24 eV and 56.5 eV are attributed to the Se $3d_{5/2}$ and $3d_{3/2}$ states emerging from spin-orbit splitting (Fig. 4e). Furthermore, the C 1s spectrum shown in Fig. 4f, reveals three discernible peaks at binding energies of 285.1, 284.5, and 286.8 eV, correlating to C=C, C–C, and C=O bonds [50]. Concurrently, the O 1s core level spectrum depicts peaks for C–O, C=O, and C–OH at binding energies of 529.2 eV, 530.3 eV, and 528.1 eV (Fig. 4g). These findings confirm the effective reduction of Se nanoparticles in the *MCL*-M@Se samples underscoring the reductive capabilities of the phytochemicals present in the *MCL* flower extract.

3.7. Urine serum biochemistry

The urinary and serum biochemical profiles were primarily utilized to elucidate the calcium oxalate (CaOx) crystal deposition in rats treated with the medications. Certainly, the derived metrics including magnesium, phosphate, oxalate, calcium, and uric acid in the urine, alongside urea nitrogen and creatinine in serum reveal the coordinated influence of the formulated drugs. In general, all the parameter in the negative control (group B) tends to be higher than other medication-treated rat groups and positive control (group A). Furthermore, the magnesium and phosphate levels in group E mirrored those of group A, highlighting the therapeutic efficacy and enhanced attenuation capability of *MCL*-M@Se NPs. In contrast, both group-C and group-D exhibited reduced levels of magnesium and phosphate relative to the negative control suggesting that both M@Se NPs and *MCL*@Se NPs medications also possess beneficial attributes as depicted in Fig. 5a&b. Additionally, the concentrations of urinary oxalate and uric acid were elevated in the negative control group indicative of kidney stone induction in comparison to the healthy control group of rats. The accumulation of urinary oxalate in renal tissue was more pronounced in the negative control group than in group A. Importantly, the

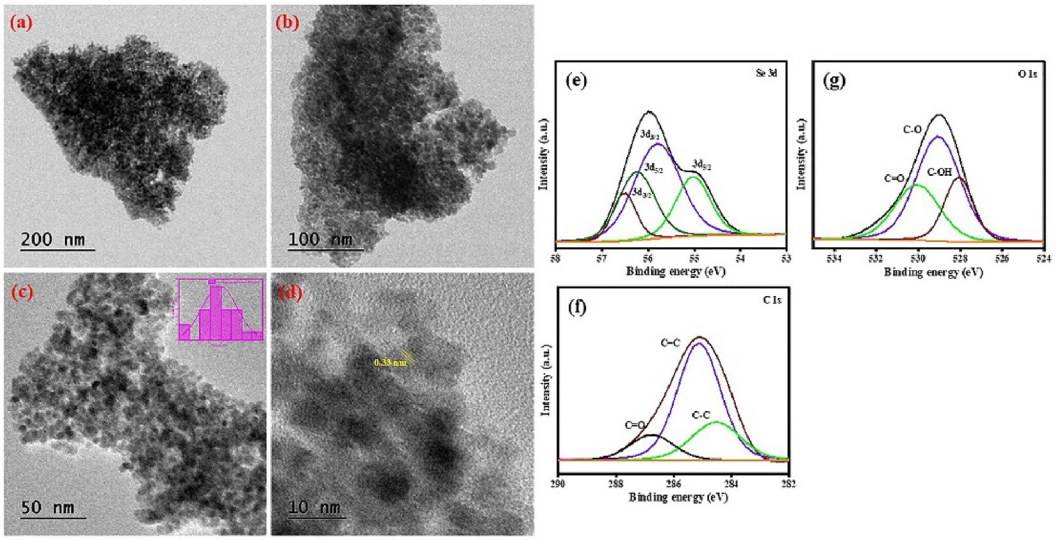

Fig. 4. HR-TEM images at various magnifications (a–d). Inset shows the particle size distribution graph as calculated from Image-J software and XPS core level spectrum of Se 3d (e), C 1s (f) and O 1s (g).

administration of *MCL*-M@Se NPs led to diminished urinary oxalate levels relative to those found in group-C and group-D rats as illustrated in Fig. 5c&d. Moreover, the patterns observed in urinary calcium levels mirrored those of urinary oxalate and uric acid concentrations. Notably, no discernible differences were found in calcium levels among group C and group D while group E manifested increased levels. This suggests that each of the medications contributed favorably to reducing calcium concentrations in urine and averting their accumulation in renal tissues, as illustrated in Fig. 5e. Our research findings emphasize that introducing *MCL*-M@Se NPs led to numerous beneficial outcomes concerning renal health. Consequentially, there was a significant reduction in the incidence of renal stones post-treatment attributable to the harmonized action of *MCL*-M@Se NPs. Moreover, enhancements in urinary biochemistry metrics signified favorable impacts on renal function. Furthermore, any structural compromises to the kidneys were rectified reinstating their inherent operational efficiency.

These results intimate that M@Se NPs, *MCL*@Se NPs, and *MCL*-M@Se NPs could serve as promising therapeutic candidates for renal-related ailments. Notably, rats treated with *MCL*-M@Se NPs medication (group-E) exhibited considerably reduced levels in comparison to group-C & D, aligning closely with the levels in the healthy control groups (group-A), as illustrated in Fig. 5f&g. When evaluating renal health levels of urea nitrogen and creatinine are frequently employed as markers of renal damage. Within the scope of this study, the group treated with CaOx *MCL*-M@Se NPs (group-E) showed notably decreased serum levels of urea nitrogen and creatinine relative to the healthy control group (group-A). Yet, when administered M@Se NPs and *MCL*@Se NPs (groups C&D), there was a marked mitigation in the elevated urea nitrogen and creatinine generation. Furthermore, it regulated the accumulation of CaOx crystals safeguarded the renal tubular epithelial cells from harm, and considerably curtailed kidney injury [51–53]. These observations bolster the contention regarding the synchronized action of *MCL*-M@Se NPs in mitigating the formation of CaOx renal stones.

3.8. Evaluation of CaOx crystals by histopathological examinations

Histological examinations using H&E, and Masson trichrome staining (MTS) were performed on renal specimens from diverse rat groups (Fig. 6). Masson staining was specifically used to

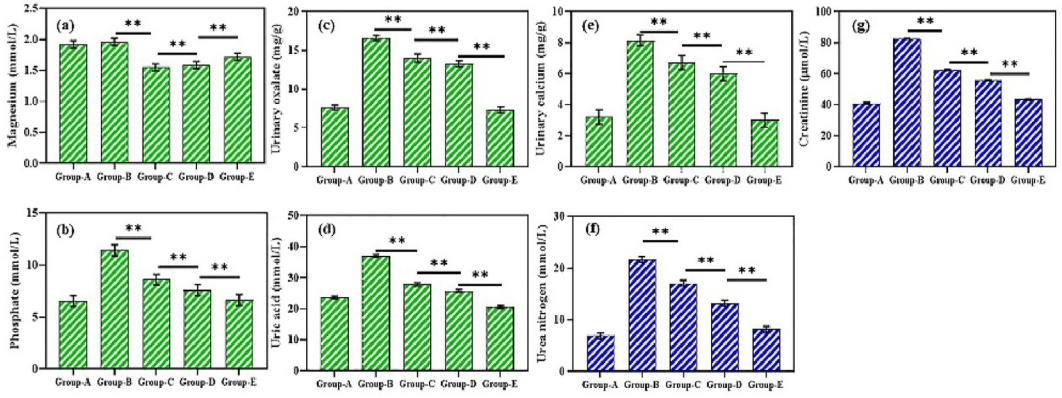

Fig. 5. Urinary magnesium (a), urinary phosphate (b), urinary oxalate (c), uric acid (d), urinary calcium (e), serum urea nitrogen (f) and creatinine (g) levels for the male Sprague Dawley rat groups (group A-E). group-A (Healthy control group), group-B (negative control group), group-C (M@Se NPs treated group), group-D (*MCL*@Se NPs treated group) and group-E (*MCL*-M@Se NPs treated group). All of the results are given as mean ± SD, with "**p < 0.01" marking significant differences compared to the group-A.

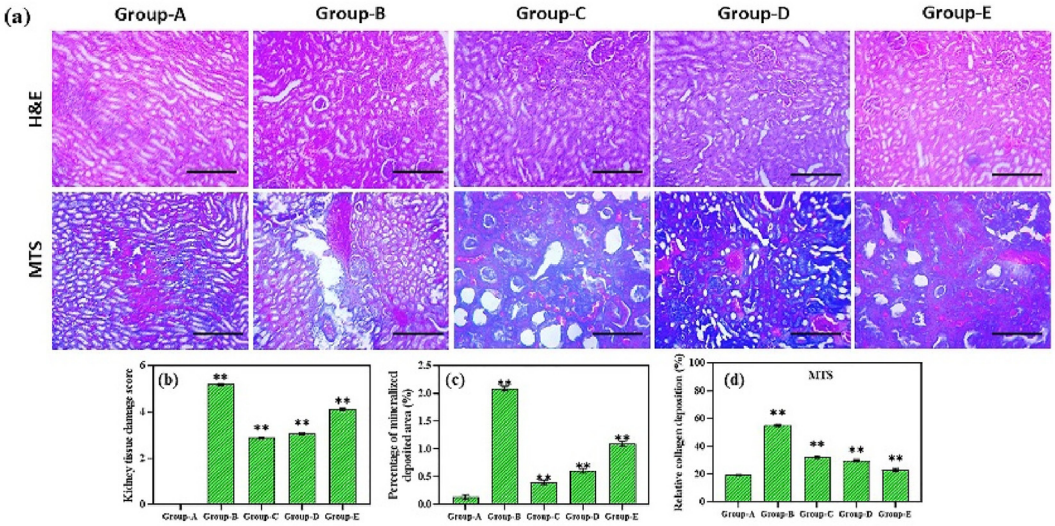

Fig. 6. Histopathological evaluations: H&E and MTS staining for Sprague Dawley rat groups (a); scale bar: 200, 100, 50, and 25 μm. Kidney tissue damage score (b), percentage of mineralized deposition area (c) and semiquantitative analysis of MTS staining (d). group-A (Healthy control group), group-B (negative control group), group-C (M@Se NPs treated group), group-D (*MCL*@Se NPs treated group) and group-E (*MCL*-M@Se NPs treated group). All of the results are given as mean ± SD, with "**p < 0.01" marking significant differences compared to the group-A.

decipher the primary pathological events leading to End-Stage Renal Disease (ESRD), Chronic Kidney Disease (CKD), and Tubulointerstitial fibrosis (TIF). Relative to the healthy control group, it was observed that rats administered with *MCL*-M@Se NPs displayed a markedly decreased accumulation of CaOx crystals compared to their counterparts treated with M@Se NPs and *MCL*@Se NPs (groups C&D). The MTS highlighted the presence of tubulointerstitial fibrosis in the kidneys of the negative control rats (group B). On the other hand, the kidneys of group A showed typical tubular structures devoid of noticeable crystal deposits. When juxtaposed with group B, a more pronounced formation of CaOx stones and clear signs of renal cell inflammation were evident. Additional findings encompassed the presence of crystal deposits capillary swelling, and dilated blood vessels within the renal tissue [54,55]. Eventually, these changes were ascertained in the formation and CaOx development in the negative control rat groups. The microscopic examinations of tissues from rats treated with *MCL*-M@Se NPs showed no signs of CaOx stone development, and both the glomerular and tubular cells exhibited typical and healthy structures. Notably, the rat groups C and D which were administered with M@Se NPs and *MCL*@Se NPs respectively, exhibited no signs of crystal deposits and retained a normal kidney cellular framework. However, slight enlargements were detected in the tubules proximate to the corticomedullary junction. These findings suggest a reduced extent of renal tissue injury marked by the absence of crystal formations and only sporadic cystic dilations within renal cells [56]. Additionally, rats treated with *MCL*-M@Se NPs displayed superior therapeutic effects showcasing intact tubules and a consistent glomerulus free from inflammation. A comparative bar chart highlighting crystal deposits indicated that the administration of *MCL*-M@Se NPs resulted in a significant reduction in CaOx deposits as opposed to treatments with M@Se NPs, *MCL*@Se NPs, and the observations from the negative control group.

Subsequent observations highlighted that the accumulation of extracellular matrix (ECM) proteins, specifically α-SMA and type-I

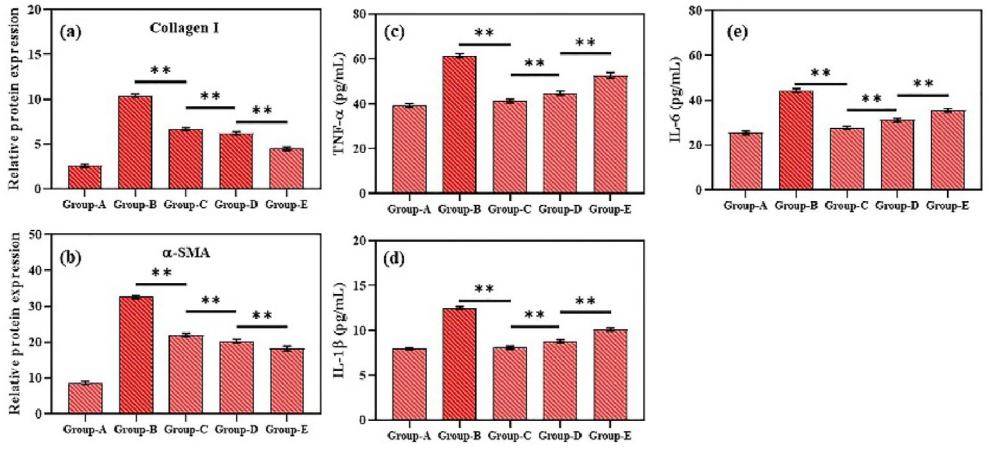

Fig. 7. Semiquantitatively for α-SMA (a), and Collagen I (b) expression levels. Levels of TNF-α (c), IL-1β (d) and IL-6 (e) in serum. group-A (Healthy control group), group-B (negative control group), group-C (M@Se NPs treated group), group-D (*MCL*@Se NPs treated group) and group-E (*MCL*-M@Se NPs treated group). All of the results are given as mean ± SD, with "**p < 0.01" marking significant differences compared to the group-A.

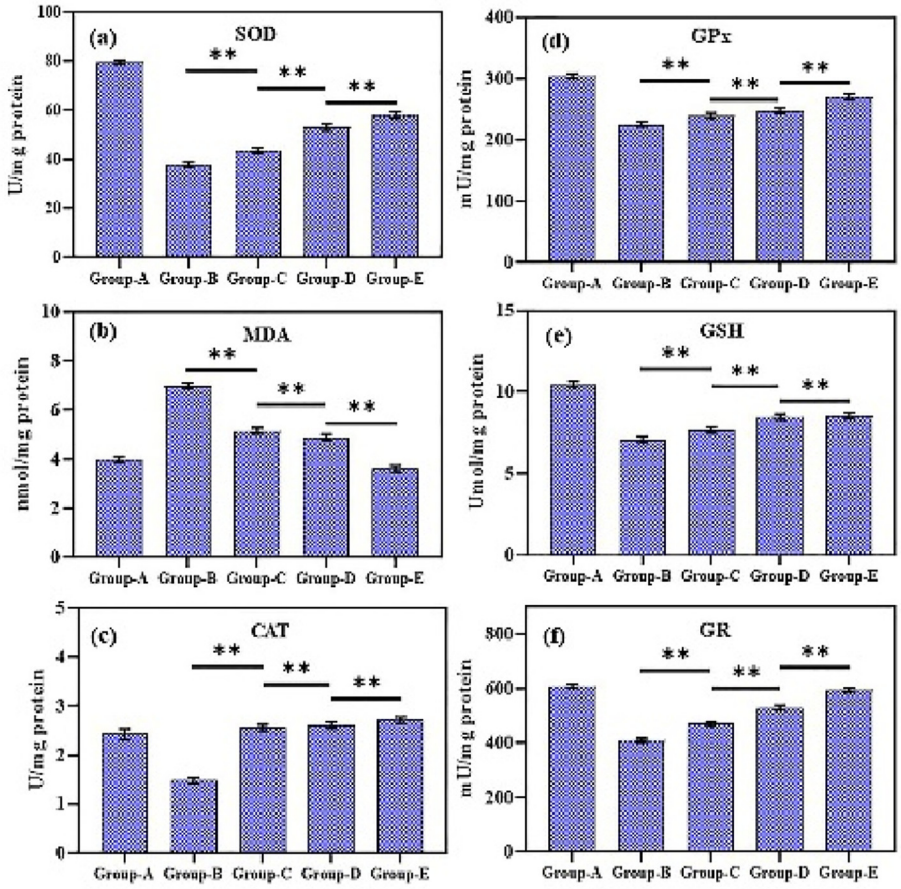

Fig. 8. SOD action (a), MDA content (b), CAT action (c), GPx action, (d) GSH levels and (e) GR actions in the male Sprague Dawley rat groups (group A-E). group-A (Healthy control group), group-B (negative control group), group-C (M@Se NPs treated group), group-D (*MCL*@Se NPs treated group) and group-E (*MCL*-M@Se NPs treated group). All of the results are given as mean ± SD, with "**p < 0.01" marking significant differences compared to the group-A.

collagen (Collagen-I) was comparable between group E and group A (Fig. 7a&b). In addition, rat groups C and D successfully curtailed renal fibrosis and ECM build-up, demonstrating outcomes akin to those seen in group B. Tubulointerstitial fibrosis (TIF), a crucial marker of advancing renal disease precipitates the deterioration of kidney functionality [57]. This degenerative process unfolds regardless of the primary instigator of renal impairment. Prolonged inflammation, stemming from a sustained injury can catalyze the onset of fibrosis. Prior studies have underscored the epithelial-mesenchymal transition (EMT) as an incipient physiological event in the evolution of nephrolithiasis [58]. Given the evidence from the present investigation, *MCL*-M@Se NPs emerge as a promising therapeutic agent for countering fibrosis especially in the scenario of ethylene glycol-induced renal stone genesis. The results suggest that *MCL*-M@Se NPs serve not just to deter the development of urolithiasis but also have a pivotal role in protecting the kidneys by mitigating the CaOx accumulations.

3.9. Oxidative stress assessment

The renal samples from group A rats (healthy control) demonstrated elevated levels of SOD, CAT, GPx, GSH, and GR while displaying diminished concentrations of MDA. In contrast, group B exhibited a pronounced increase in MDA and a concomitant decrease in levels of SOD, CAT, GPx, GSH, and GR. Notably, this study underscores that the combined effects of *MCL*-M@Se NPs significantly diminish the levels of SOD, CAT, GPx, GSH, and GR, thereby elevating MDA concentrations relative to group B. Nevertheless, the groups treated with synthesized M@Se NPs and *MCL*@Se NPs (group-C & D) also presented with a marked reduction in CaOx stone formation comparable to the results observed in group-B (Fig. 8). The adherence of CaOx crystals to tubular epithelial cells catalyzes the activation of NADPH oxidase. This in turn, results in the generation of superoxide prompting the activation of cyclophilin D. This cascade ultimately promotes mitochondrial permeability transition (MPT) within renal tissues [59]. Such stimulation instigates alterations in the mitochondrial transmembrane potential culminating in mitochondrial destabilization. This process facilitates the release of cytochrome *c* into the cytoplasm. Moreover, this release triggers apoptosis, and the subsequent discharge of ROS into the cytosol inflicts additional harm on the epithelial cells [60,61]. The oxidative stress-induced damage to these cells is considered pivotal for renal calculus formation, and this process appears to be potentiated by *MCL*-M@Se NPs. The onset of renal damage due to hyperoxaluria is rooted in the oxidative stress pathway potentially resulting in an augmented accumulation of CaOx within the kidneys. The *MCL* flower extract is renowned for its potent antioxidant properties. The incorporation of the metformin drug further amplifies this antioxidant capability thereby boosting its effectiveness. Additionally, the *MCL* flower extract in tandem with metformin serves as a potent agent in alleviating oxidative stress in the Sprague Dawley rat model. Significantly, the synergistic action of Se NPs with this established combination has been shown to diminish CaOx deposition, thereby mitigating renal tissue

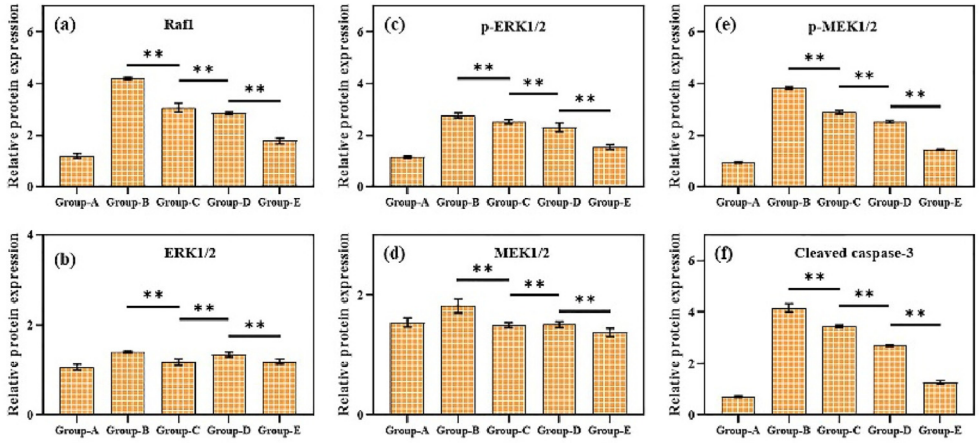

Fig. 9. Relative protein expression of Raf1 (a), ERK1/2 (b), p-ERK1/2 (c), MEK1 (d), p-MEK1 (e) and Cleaved caspase-3 (f) in the male Sprague Dawley rat groups (group A-E). The protein band calculated as a ratio relative to β-actin protein levels. group-A (Healthy control group), group-B (negative control group), group-C (M@Se NPs treated group), group-D (*MCL*@Se NPs treated group) and group-E (*MCL*-M@Se NPs treated group). All of the results are given as mean ± SD, with "**p < 0.01" marking significant differences compared to the group-A.

damage. The present study underscores that Se NPs combined with metformin can counteract the oxidative stress instigated by glyoxylate administration. Notably, the fusion of *MCL* flower extract with Se NPs and metformin curtails the heightened oxidative stress induced by Se NPs alone positioning the *MCL*-M@Se NPs as the most efficacious treatment.

3.10. MCL-M@Se NPs effects on inflammatory factors and MAPK pathway

In the control cohorts of rats where no treatment was administered, there was a discernible augmentation in the serum concentrations of TNF-α, IL-1β, and IL-6 (Fig. 7c–e). Contrarily, group A along with other rat cohorts demonstrated diminished levels of these inflammatory markers. Most strikingly, rats that underwent treatment with *MCL*-M@Se NPs manifested the most attenuated levels underscoring the potent synergistic efficacy of the medication. To delve deeper into the intricacies of the MAPK signaling cascade investigators probed the protein expression profiles of Raf1, ERK1/2, p-ERK1/2, MEK1/2, p-MEK1/2, and cleaved caspase-3 (Fig. 9a–f). The research also gauged the relative transcriptional activity of six genes: C-Raf, MAPK1, MAPK3, MAP2K1, MAP2K2, and CASP-3 which are concomitant with the aforementioned proteins (Fig. 10a–f). Rats in the pinnacle of health from group A exhibited the most subdued levels of these proteins and associated mRNA transcription. Conversely, group B presented with markedly augmented mRNA and protein profiles. Noteworthily, group-E manifested diminished levels of relative mRNA and protein expression analogous to cohorts treated with medications (group C&D). These findings compellingly indicate that the introduction of *MCL*-M@Se NPs mitigated inflammatory indices and quelled the activity of the MAPK signaling axis in kidney stone-afflicted Sprague Dawley rats.

The MAPK signaling cascade activated by a range of external and internal stimuli such as oxidative stress, inflammation, and ROS, principally modulates oxidative distress, inflammation, and cellular harm. Our investigation highlighted amplified serum concentrations of inflammatory indicators (TNF-α, IL-1β, IL-6), enhanced protein expression of Raf1, ERK1/2, p-ERK1/2, MEK1/2, p-MEK1/2, and cleaved caspase-3. Additionally, there was an upsurge in the transcriptional activity of genes like C-Raf, MAPK1, MAPK3, MAP2K1, MAP2K2, and CASP-3 in the untreated control cohort

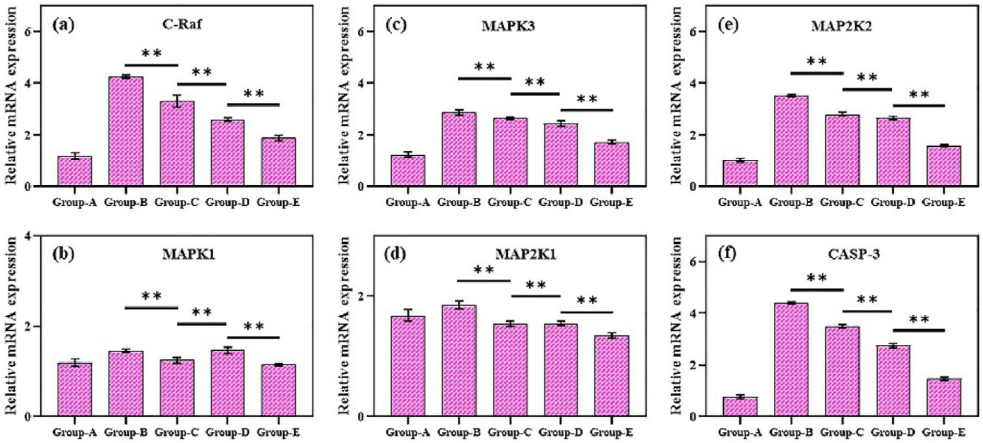

Fig. 10. Relative mRNA expression of C-Raf (a), MAPK1 (b), MAPK3 (c), MAP2K1 (d), MAP2K2 (e), and CASP-3 (f) genes in the male Sprague Dawley rat groups (group A-E) by qRT-PCR. group-A (Healthy control group), group-B (negative control group), group-C (M@Se NPs treated group), group-D (*MCL*@Se NPs treated group) and group-E (*MCL*-M@Se NPs treated group). All of the results are given as mean ± SD, with "**p < 0.01" marking significant differences compared to the group-A.

(group B). This points to a pronounced activation of the MAPK cascade. Intriguingly, the administration of *MCL*-M@Se NPs to rats in group E (afflicted with calcium oxalate stones) curtailed the MAPK signaling, diminished the inflammatory indicators, and decreased the protein and mRNA transcriptional activity [62,63]. Selenium nanoparticles combined with *MCL* flower extract and metformin drug hinder the activation of MAPK by disrupting the function of signaling molecules that are located upstream such as Raf1 and MEK1/2. In addition, studies have demonstrated that selenium compounds can reduce the transcriptional activity of genes involved in the MAPK pathway such as MAPK1 and MAPK3 [64,65]. The use of selenium in *MCL*-M@Se NPs treatment has a dual effect on the MAPK pathway affecting both protein expression and gene transcription. This scientific basis explains the observed anti-inflammatory and anti-apoptotic benefits of the treatment in reducing inflammation associated with CaOx stone formation.

The combination of Metformin, Se NPs, and *Myrtus communis* L. flower extract has the potential to be an effective method for reducing CaOx deposition in the kidneys of Male Sprague Dawley Rats. Se NPs have strong antioxidant characteristics which are essential for countering oxidative stress that is involved in the production of kidney stones. The flower extract of *Myrtus communis* L. which contains high levels of flavonoids and polyphenols enhances these effects by providing anti-inflammatory and nephroprotective characteristics. This collaborative method improves the effectiveness of Metformin as a medicine as demonstrated by studies that highlight the superior advantages of Se NPs and *Myrtus communis* L. extract in promoting kidney health. This comprehensive therapy focuses on addressing the fundamental processes involved in the development of calcium oxalate kidney stones in contrast to conventional treatments like Thiazide diuretics, Allopurinol, and Potassium citrate, which mainly provide temporary relief from symptoms. Furthermore, the combination of these elements may result in the ability to use smaller amounts reducing negative consequences while maximizing the inherent benefits of herbal extracts when mixed with metal nanoparticles. This infers that *MCL*-M@Se NPs could potentially modulate the MAPK cascade in rats bearing CaOx stones. The research further accentuates the efficacy of *MCL* flower extract with metformin and Se NPs as an efficacious remedy for renal impairment. This targeted approach against the MAPK cascade heralds a groundbreaking therapeutic strategy for urolithiasis.

4. Conclusion

In summary, our research suggests that a specific combination of *MCL* flower extract, the drug metformin, and Se NPs at a ratio of 1:1.5:1 can potentially counteract CaOx stone formation in Sprague Dawley rats given 1% and 2% solutions of ethylene glycol and ammonium chloride. The XRD analysis indicates that the synthesized selenium nanoparticles have a crystalline size of around 48 nm, and this is in good agreement with JCPDS No: 06-0362. The HR-TEM investigation ultimately determines that the average size of Se NPs in *MCL*-M@Se NPs is 13.8 nm. Additionally, the XPS spectrum strongly indicates the presence of selenium nanoparticles in the 3d state. The presence of two peaks at energy levels of 55.03 eV and 55.79 eV can be attributed to the Se $3d_{5/2}$ and $3d_{3/2}$ states. Analysis from urine serum biochemistry and histopathology confirms that this *MCL*-M@Se NPs blend significantly reduced CaOx accumulation in renal tissues. Additionally, rats treated with this combination showed reduced serum levels of inflammatory markers like TNF-α, IL-1β, and IL-6. This treatment also decreased urine levels of Mg, Ph, Ox, Ca, and uric acid, along with serum levels of urea nitrogen and creatinine. Further investigation into protein and mRNA expressions linked the benefits of *MCL*-M@Se NPs to the suppression of the MAPK signaling pathway. Thus, this research introduces an optimized *MCL*-M@Se NPs combination (1:1.5:1) as a promising approach to combat CaOx stone formation and related kidney damage.

Ethical approval

Animal experiments were performed in care with the National Research Council (US) Committee for Guide for the Care and Use of Laboratory Animals and all animal experiments were carried out after approval from the Institutional Animal Ethics Committee of The Affiliated Hospital to Changchun University of Chinese Medicine, PR China.

Consent to participate

All of the authors agree to work on this project.

Consent to publish

All authors have given their consent to publish the manuscript. The manuscript has not been previously published and is not currently being reviewed by any other journal.

Authors' contributions

Jian Kang - Experimental design, Data Analysis, Data interpretation; Yanqing Tong – Drafted manuscript and principal investigation.

All authors read and approved the final manuscript.

Funding

This study was supported by the National Natural Science Foundation of China (Project No.: 81374039, 81873070).

Data availability statement

Data will be made available on request. This published article and its supplementary information files include all the data generated or analyzed during the study.

Declaration of competing interest

The authors declare that there is no conflict of interest.

Acknowledgments

None.

References

[1] Geraghty RM, Davis NF, Tzelves L, Lombardo R, Yuan C, Thomas K, et al. Best practice in interventional management of urolithiasis: an update from the European association of urology guidelines panel for urolithiasis 2022. Eur Urol Focus 2023;9:199–208.

[2] Tripathi D, Misra A, Chaudhary MK, Srivastava S. Evaluation of Coscinium fenestratum (Goetgh.) Colebr. stem extracts for urolithiasis and quantification of bioactive alkaloids to validate the traditional claims. Nat Prod Res 2023;37:2894–9.

[3] Shaheen S, Khalid S, Siqqique R, Abbas M, Ifikhar T, Ijaz I, et al. Comparative taxonomical, biological, and pharmacological potential of healthy and geminivirus infected leaves of Hibiscus rosa-sinensis L.: first report. Biol Pharmacol Potential Heal Geminivirus Infected Leaves Hibiscus Rosa-Sinensis L First Rep n.d 185:106428.

[4] Nagarjun Batchu SRI, Ganesh Yerra V, Hong Y, Plant P, Liu Y, Advani A. 397-P: Epigenetic regulation of the chemokine CXCL2 in acute kidney injury in diabetes. Diabetes 2023;72.

[5] Bishoyi SK, Tripathy UP. Ethnomedicinal plants used in kidney stones and infection of the urinary tract by the tribal community of Rayagada District, Odisha. Int J Sci Res Arch 2023;8:102–16.
[6] Hariri G, Collet L, Duarte L, Martin GL, Resche-Rigon M, Lebreton G, et al. Prevention of cardiac surgery-associated acute kidney injury: a systematic review and meta-analysis of non-pharmacological interventions. Crit Care 2023;27:1–13.
[7] Khalid S, Arshad M, Raza K, Mahmood S, Siddique F, Aziz N, et al. Assessment of hepatoprotective, nephroprotective efficacy, and antioxidative potential of Moringa oleifera leaf powder and ethanolic extract against PCOS-induced female albino mice (Mus Musculus). Food Sci Nutr 2023;11:7206–17.
[8] Mahammad A-M, Tekou FA, Woumbo CY, Kentsop MP, Djuine V, Kuate D. Simultaneous consumption of green and black tea infusions from Cnidoscolus aconitifolius leaves with metformin treatment improves the health outcome in type II diabetic rats. CyTA - J Food 2023;21:386–93.
[9] Du F, Liu M, Wang J, Hu L, Zeng D, Zhou S, et al. Metformin coordinates with mesenchymal cells to promote VEGF-mediated angiogenesis in diabetic wound healing through Akt/mTOR activation. Metabolism 2023;140:155398.
[10] Chen B, He Q, Yang J, Pan Z, Xiao J, Chen W, et al. Metformin suppresses oxidative stress induced by high glucose via activation of the Nrf2/HO-1 signaling pathway in type 2 diabetic osteoporosis. Life Sci 2023;312:121092.
[11] Sri L, Orsu P. Early diagnosis through estimation of inflammatory biomarkers and the neuroprotective role of metformin in diabetic peripheral neuropathy. Int J Pharm Sci Nanotechnol 2023;16:6427–37.
[12] Abdelgawad IY, Agostinucci K, Sadaf B, Grant MKO, Zordoky BN. Metformin mitigates SASP secretion and LPS-triggered hyper-inflammation in Doxorubicin-induced senescent endothelial cells. Front Aging 2023;4:1170434.
[13] Patel T, Nageeta F, Sohail R, Butt TS, Ganesan S, Madhurita F, et al. Comparative efficacy and safety profile of once-weekly Semaglutide versus once-daily Sitagliptin as an add-on to metformin in patients with type 2 diabetes: a systematic review and meta-analysis. Ann Med 2023;55:2239830.
[14] Melin J, Forslund M, Alesi S, Piltonen T, Romualdi D, Spritzer PM, et al. The impact of metformin with or without lifestyle modification versus placebo on polycystic ovary syndrome: a systematic review and meta-analysis of randomized controlled trials. Eur J Endocrinol 2023;189:S37–63.
[15] Susilawati E, Levita J, Susilawati Y, Sumiwi SA. Review of the case reports on metformin, sulfonylurea, and thiazolidinedione therapies in type 2 diabetes mellitus patients. Med Sci 2023;11:50.
[16] Zakaria NH, Majid FAA, Helmi NANM, Fadhlina A, Sheikh HI. Medicinal potentials of Strobilanthes crispus (L.) and Orthosiphon stamineus Benth. in the management of kidney stones: a review and bibliometric analysis. J Herb Med 2023:100773.
[17] Mehrabi S, Beigi P, Salehpour Z. Comparison of the effect of hydroalcholic extract of alhagi maurorum and hydrochlorothiazide on excretion of 4–10 mm kidney and ureteral stones in adults: a randomized prospective study. Adv Pharmacol Pharm Sci 2023;2023.
[18] Rajeshwari T, Suresh R, Sudhakar M. Anti-urolithiatic activity of saponin rich fraction from the methanolic extract of Achyranthes aspera against ethylene glycol induced urolithiasis in Wistar rats. J Appl Pharmaceut Sci 2023;13:197–203.
[19] Belahcene S, Kebsa W, Omoboyowa DA, Alshihri AA, Alelyani M, Bakkour Y, et al. Unveiling the chemical profiling antioxidant and anti-inflammatory activities of Algerian Myrtus communis L. Essential oils, and exploring molecular docking to predict the inhibitory compounds against cyclooxygenase-2. Pharmaceuticals 2023;16:1343.
[20] Nenni M, Karahüseyin S. Antioxidant capacity of essential oils obtained from Myrtus communis L. And citrus sinensis (L.) osbeck plants widely consumed in adana region. Cumhur Sci J 2023;44:470–3.
[21] Islim Y, Muhammad D. Antibacterial study of the Ethanolic extract of local common Myrtle leaves Myrtus communis L.(Myrtaceae). Res J Pharm Technol 2023;16:3941–4.
[22] Dabravolski SA, Sukhorukov VN, Melnichenko AA, Khotina VA, Orekhov AN. Potential application of the plant-derived essential oils for atherosclerosis treatment: molecular mechanisms and therapeutic potential. Molecules 2023;28:5673.
[23] Yang BY, Zhao MS, Lv JC, Wang XC, Zhao YQ, Li J, et al. Porous Se@ SiO2 nanospheres inhibit calcium oxalate kidney stone formation by oxidation resistance. Ceram Int 2023;49:8856–62.
[24] Lazcano-Ramírez HG, Garza-García JJO, Hernández-Díaz JA, León-Morales JM, Macías-Sandoval AS, García-Morales S. Antifungal activity of selenium nanoparticles obtained by plant-mediated synthesis. Antibiotics 2023;12:115.
[25] Hashem AH, Saied E, Ali OM, Selim S, Al Jaouni SK, Elkady FM, et al. Pomegranate peel extract stabilized selenium nanoparticles synthesis: promising antimicrobial potential, antioxidant activity, biocompatibility, and hemocompatibility. Appl Biochem Biotechnol 2023:1–24.
[26] Saranya T, Ramya S, Kavithaa K, Paulpandi M, Cheon Y-P, Harysh Winster S, et al. Green synthesis of selenium nanoparticles using solanum nigrum fruit extract and its anti-cancer efficacy against triple negative breast cancer. J Cluster Sci 2023;34:1709–19.
[27] Dhanraj G, Rajeshkumar S. Anticariogenic effect of selenium nanoparticles synthesized using Brassica oleracea. J Nanomater 2021;2021. https://doi.org/10.1155/2021/8115585.
[28] Gunti L, Dass RS, Kalagatur NK. Phytofabrication of selenium nanoparticles from emblica officinalis fruit extract and exploring its biopotential applications: antioxidant, antimicrobial, and biocompatibility. Front Microbiol 2019;10:1–17. https://doi.org/10.3389/fmicb.2019.00931.
[29] Vundela SR, Kalagatur NK, Nagaraj A, Kadirvelu K, Chandranayaka S, Kondapalli K, et al. Multi-biofunctional properties of phytofabricated selenium nanoparticles from Carica papaya fruit extract: antioxidant, antimicrobial, antimycotoxin, anticancer, and biocompatibility. Front Microbiol 2022;12:1–19. https://doi.org/10.3389/fmicb.2021.769891.
[30] Banerjee M, Rajeswari VD. Green synthesis of selenium nanoparticles using leaf extract of Moringa oleifera, their biological applications, and effects on the growth of Phaseolus vulgaris-: agricultural synthetic biotechnology for sustainable nutrition. Biocatal Agric Biotechnol 2024;55:102978.
[31] Tamanna IS, Gayathri R, Sankaran K, Veeraraghavan VP, Francis AP. Eco-friendly synthesis of selenium nanoparticles using Orthosiphon stamineus leaf extract and its biocompatibility studies. Bionanoscience 2024;14:37–44.
[32] EL-Shafey N, Mustafa NH, El-Shekih AA. Cytotoxic effects of zinc oxide nanoparticles and ethanolic extract of mureer plant in renal tissue via apoptosis mechanism induction with the promising protective role of gallic acid in rats. Bull Fac Sci Zagazig Univ 2023;2022:20–30.
[33] Han M, Wang S, Zhou X, Zhang P, Han Z, Chen Y, et al. Baicalin alleviates bleomycin-induced early pulmonary fibrosis in mice via the mitoKATP signaling pathway. Toxicology 2023:153638.
[34] Xu X, Yu Y, Ling M, Ares I, Martínez M, Lopez-Torres B, et al. Oxidative stress and mitochondrial damage in lambda-cyhalothrin toxicity: a comprehensive review of antioxidant mechanisms. Environ Pollut 2023:122694.
[35] Tian Y, Zhao J, Chen L, Zhang C, Chu X, Xia Y. Sanjin Paishi Decoction improves the imbalance of gut microbiota and regulates MAPK signaling pathway to inhibit calcium oxalate stones in rats. Int Urol Nephrol 2023;55:2421–9.
[36] Gao Y, Mo S, Cao H, Zhi Y, Ma X, Huang Z, et al. The efficacy and mechanism of Angelica sinensis (Oliv.) Diels root aqueous extract based on RNA sequencing and 16S rDNA sequencing in alleviating polycystic ovary syndrome. Phytomedicine 2023;120:155013.
[37] Abuderman AA, Syed R, Alyousef AA, Alqahtani MS, Ola MS, Malik A. Green synthesized silver nanoparticles of Myrtus communis L (AgMC) extract inhibits cancer hallmarks via targeting aldose reductase (AR) and associated signaling network. Processes 2019;7. https://doi.org/10.3390/pr7110860.
[38] Menon S, Agarwal H, Shanmugam VK. Catalytical degradation of industrial dyes using biosynthesized selenium nanoparticles and evaluating its antimicrobial activities. Sustain Environ Res 2021;31. https://doi.org/10.1186/s42834-020-00072-6.
[39] Ghosh M, Mandal S, Paul S, Chakrabarty S, Roy A, Chakrabarti G, et al. Synthesis and characterization of metformin conjugated magnetic nanocomposite with enhanced activity against the human carcinoma cells. J Drug Deliv Sci Technol 2023;87:104781.
[40] Dhouibi I, Flamini G, Bouaziz M. Comparative study on the essential oils extracted from Tunisian rosemary and myrtle: chemical profiles, quality, and antimicrobial activities. ACS Omega 2023;8:6431–8.
[41] Bhoi RT, Bhoi CN, Nikume SR, Bendre RS. Design, synthesis, and in silico studies of benzimidazoles of thymol as potent antiplasmodial and antimicrobial agents. Results Chem 2023:101112.
[42] Hou T, Guo Y, Han W, Zhou Y, Netala VR, Li H, et al. Exploring the biomedical applications of biosynthesized silver nanoparticles using perilla frutescens flavonoid extract: antibacterial, antioxidant, and cell toxicity properties against colon cancer cells. Molecules 2023;28:6431.
[43] Kokila K, Elavarasan N, Sujatha V. Diospyros Montana leaf extract-mediated synthesis of selenium nanoparticles and their biological applications. New J Chem 2017;41:7481–90. https://doi.org/10.1039/c7nj01124e.
[44] Mohammed JS, Hasan MA, Alatta HJ, Abd-AL Majied MI, Jasim KA, Shaban AH, et al. Investigate the structural properties of Tl1-xHgxSr2Ca2Cu3O8+ δ compound by using Scherrer modified equation. AIP Conf Proc 2023;2769. AIP Publishing.
[45] Patil NA, Udgire S, Shinde DR, Patil PD. Green synthesis of gold nanoparticles using extract of Vitis vinifera, Buchananialanzan, Juglandaceae, Phoenix Dactylifera plants, and evaluation of antimicrobial activity. Chem Methodol 2023;7:15–27.
[46] Sanjivkumar M, Silambarasan TS. Exploration on green synthesis of nanoparticles from plants and microorganisms and their biological applications. Mod. Nanotechnol. Vol. 2 Green Synth. Sustain. Energy impacts. Springer; 2023. p. 149–73.
[47] Sayed R, M Elmasri M, Dhmees AS. A comparative study of particle size measurement of silver, gold and silica sand nanoparticles with different nanometrological techniques. Egypt J Chem 2023;66:385–93.
[48] Gaber SE, Hashem AH, El-Sayyad GS, Attia MS. Antifungal activity of mycosynthesized bimetallic ZnO-CuO nanoparticles against fungal plant pathogen Fusarium oxysporum. Biomass Convers Biorefinery 2023:1–15.
[49] Zhan B, Butt S, Liu Y, Le Lan J, Nan CW, Lin YH. High-temperature thermoelectric behaviors of Sn-doped n-type Bi2O2Se ceramics. J Electroceram 2015;34:175–9. https://doi.org/10.1007/s10832-014-9969-2.
[50] Sun Y, Shi Y, Jia H, Ding H, Yue T, Yuan Y. Biosynthesis of selenium nanoparticles of Monascus purpureus and their inhibition to Alicyclobacillus acidoterrestris. Food Control 2021;130:108366. https://doi.org/10.1016/j.foodcont.2021.108366.
[51] Sun Y, Kang J, Tao Z, Wang X, Liu Q, Li D, et al. Effect of endoplasmic reticulum stress-mediated excessive autophagy on apoptosis and formation of kidney stones. Life Sci 2020;244:117232. https://doi.org/10.1016/j.lfs.2019.117232.

[52] Kang J, Sun Y, Deng Y, Liu Q, Li D, Liu Y, et al. Autophagy-endoplasmic reticulum stress inhibition mechanism of superoxide dismutase in the formation of calcium oxalate kidney stones. Biomed Pharmacother 2020;121:109649. https://doi.org/10.1016/j.biopha.2019.109649.
[53] Li X, Wang W, Su Y, Yue Z, Bao J. Inhibitory effect of an aqueous extract of Radix Paeoniae Alba on calcium oxalate nephrolithiasis in a rat model. Ren Fail 2017;39:120–9. https://doi.org/10.1080/0886022X.2016.1254658.
[54] Zhao F, Yang T, Zhou L, Zhao J, Liu J, Ping W, et al. Construction of tissue-engineered bladders using an artificial acellular nanocomposite scaffold loaded with stromal vascular fraction secretome. Acta Biomater 2023;167:260–77.
[55] Naguib YW, Alhaj-Suliman SO, Wafa EI, Saha S, Ebeid K, Mohammed HHH, et al. Ciprofloxacin derivative-loaded nanoparticles synergize with paclitaxel against type II human endometrial cancer. Small 2023:2302931.
[56] Das A, Mead P, Sayer JA. Adult presentations of variable kidney and liver phenotypes secondary to biallelic PKHD1 pathogenic variants. J Rare Dis 2023;2:1.
[57] Wu S, Yan M, Liu J, Li Y, Tian R, Li C, et al. Clerodendranthus spicatus inhibits epithelial–mesenchymal transition of renal tubular cells through the NF-κB/Snail signalling pathway in hyperuricaemia nephropathy. Pharm Biol 2023;61:1274–85.
[58] Chung Y-H, Huang G-K, Kang C-H, Cheng Y-T, Kao Y-H, Chien Y-S. MicroRNA-26a-5p restoration ameliorates unilateral ureteral obstruction-induced renal fibrosis in mice through modulating TGF-β signaling. Lab Invest 2023;103:100131.
[59] Kaur M, Bhatia S, Sangha MK, Phutela UG. Crosstalk of AsA/DHA and GSH/GSSG ratios' role in growth-phase dependent antioxidative defense in euryhaline and freshwater microalgae: explored for the first time. Physiol Mol Biol Plants 2023:1–18.
[60] Barwal SK, Goutam C, Chauhan C, Vimala Y, Alyemeni MN, Ahmad P, et al. Salicylic acid alleviates salt-induced phytotoxicity by modulating physiochemical attributes and upregulating the AsA-GSH cycle and glyoxalase system in Capsicum annuum L. seedlings. South Afr J Bot 2023;161:222–37.
[61] Banaee M, Badr AA, Multisanti CR, Haghi BN, Faggio C. The toxicity effects of the individual and combined exposure of methyl tert-butyl ether (MTBE) and tire rubber powder (RP) on Nile tilapia fish (Oreochromis niloticus). Comp Biochem Physiol, Part C: Toxicol Pharmacol 2023:109759.
[62] Yang Y, Wang Q, Xun Y, Li C, Wang S. The preliminary exploration of what role miRNAs derived from urinary exosomes play in kidney stone formation. Urology 2022;166:104–10.
[63] Zhang S, Zhu J, Ju Y, Lv M, Yang R, Li Y, et al. Drosophila model and network pharmacology to explore novel targets and novel active components of Chinese traditional medications for treating kidney stones. Pharmacol Res Chinese Med 2023;6:100220.
[64] Jiang J, Cui X, Huang Y, Yan D, Wang B, Yang Z, et al. Advances and prospects in integrated nano-oncology. Nano Biomed Eng 2024;16:152–87.
[65] Shekhar A, Singh S, Gupta K, Rai AK, Tewari RP. Comprehensive review of available nanotechnological techniques for treating nonsolid tumors. Nano Biomed Eng 2023;15:191–8. https://doi.org/10.26599/NBE.2023.9290023.